Modeling lightweight cemented backfill considering progressive breakage

Chengjun Yu[1], An Deng[1*], Giang Nguyen[1]

[1] School of Civil, Environmental and Mining Engineering

University of Adelaide

Adelaide, SA 5005, Australia.

[*] Corresponding Author

Correspondence to email address: an.deng@adelaide.edu.au

Abstract: An analytical model for lightweight cemented backfill is presented. The model integrates elastic-brittle and elastic-plastic components, replicating responses of low-density materials and cementation that are present in backfills. The model uses a semi-implicit algorithm to iterate stress−strain solutions, and the universal shear contraction. The model was validated on a lightweight cemented backfill containing expanded polystyrene beads.

Keywords: constitutive; elasto–brittle; elasto–plastic; modified Cam Clay; breakage; yield surface

1. Introduction

Cemented backfills with low-density inclusions have been recognized as valuable substitutes for compacted soils [1-7]. These backfills offer favorable properties (e.g., lighter weight and improved ductility) that compacted soils rarely exhibit. Due to cement inclusions, the backfills are brittle and behave like a soft rock or hard soil [8, 9]. The low-density inclusions are compressible, enabling material ductility. The brittle–ductile nature complicates infrastructure design and performance optimization. Neglecting it does not acknowledge the material nature and will under- or overdesign infrastructures that involve the backfills. A better solution is to consider, from material modeling perspective, the effects arising from material cementation and ductility.

Cementation affects yield surface. Gens and Nova [10] suggested to enlarge the yield surface of the base soil. This approach was redeveloped by Rahimi *et al.* [11] who upscaled the yield locus without changing its shape. The approaches are valid where the cementation governs the behavior [12]. Stress−strain relationships are also affected, mainly due to the presence of inclusions. The inclusions such as expanded polystyrene (EPS) beads or rubber particles are lightweight but compressible. In these settings, the backfills contract noticeably when sheared, as opposed to shear dilation or light contract occurred to non-inclusion backfills. The impact on shear behavior has been recognized in [5]. Similar modeling challenges were reported in [13-16] which likewise applied compressible inclusions to materials. To these ends, the material ductility should be considered by developing more advanced modelling work.

2. Model Development

2.1 Conception

A cemented material, if loaded, exhibits two components of strength: cementation bonds and granular frictions. The cementation is progressively damaged during loading; the material turns gradually into an assembly of granular material. In this context, the bonds and frictions share, in changing ratios, the loads. When the bonds diminish, the frictions, as of usual granular materials, continue to withstand the load until the material reaches failure. We calibrated the bond−friction relationship using a hybrid model, i.e., an elasto-brittle body for the pre-breakage, and an elasto-plastic body post the breakage. Specifically, at the early stage of loading, the material withstands the loads mainly through the elasto-brittle body. The elasto-plastic body comes into effect when the cementation breakage occurs.

As in [17], the elastic, brittle and plastic behaviors are represented respectively by a set of mechanical elements, i.e., a spring, a bonded bar and a slider as shown in Figure 1. The corresponding moduli are elastic modulus, K, yield strength, f_y, and break strength, q_u. The elasto-brittle body is represented by a spring and a bonded bar connected in series; and the elasto-plastic body by a spring and a slider in series, as show in Figure 2. The two bodies are paired in parallel to share the load, P. The share ratio is stress-dependent and is determined as a function of cementation breakage.

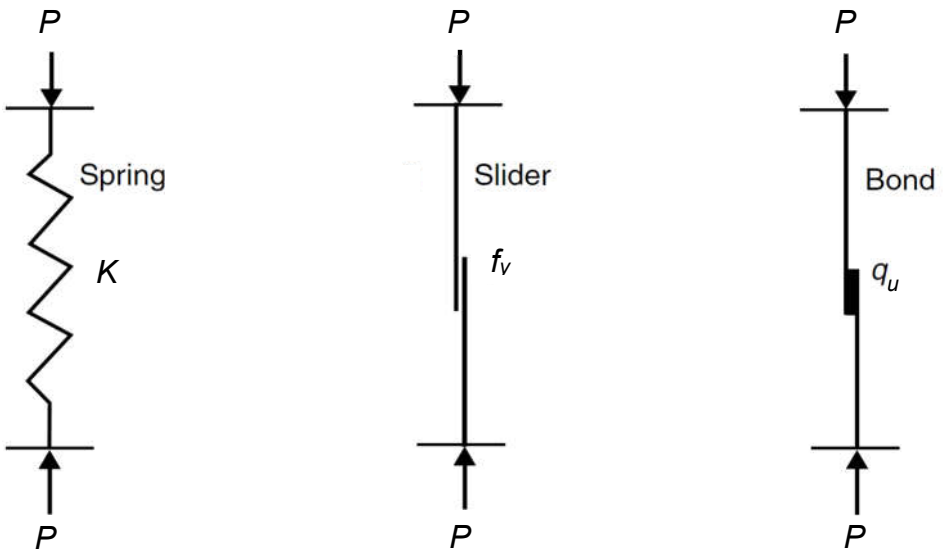

(a) (b) (c)

Figure 1 Diagrams of mechanic elements defined to simulate (a) elastic, (b) plastic and (c) brittle behaviors of material.

65

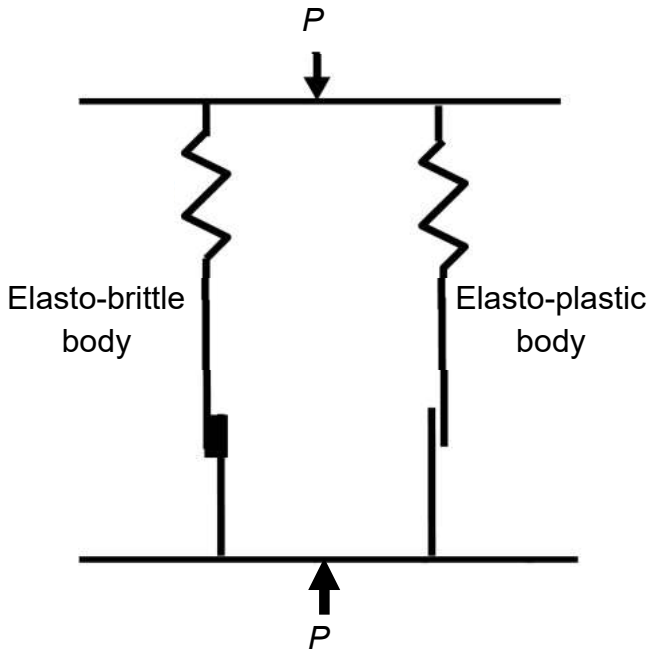

Figure 2 Diagram of a parallel unit defined to represent concurrent elasto-brittle and elasto-plastic responses of material.

66

2.2 Model Details

The model assumes slowly compressed stress conditions and perfectly drained conditions, thus enabling the total stress analysis. The model defines a set of stress and strain parameters in drained. The mean stress, p, and the deviatoric stress, q, are expressed as:

$$p = \frac{1}{3}(\sigma_1 + \sigma_2 + \sigma_3) \tag{1}$$

$$q = \frac{1}{\sqrt{2}}((\sigma_1 - \sigma_2)^2 + (\sigma_2 - \sigma_3)^2 + (\sigma_3 - \sigma_1)^2) \tag{2}$$

where σ_1, σ_2 and σ_3 are the major, intermediate and minor principal stresses, respectively. In a standard triaxial stress space, $\sigma_2 = \sigma_3$. The corresponding volumetric strain increment, $\partial\varepsilon_v$, and shear strain increment, $\partial\varepsilon_s$, respectively are:

$$\partial\varepsilon_v = \partial\varepsilon_1 + 2\partial\varepsilon_3 \tag{3}$$

$$\partial\varepsilon_s = \frac{2(\partial\varepsilon_1 - \partial\varepsilon_3)}{3} \tag{4}$$

where ε_1 and ε_3 are the major and minor principal strains, respectively.

The stresses, p and q, and strain, ε, are shared by the elasto-brittle body and the elasto-plastic body as in Figure 2. In terms of homogenization method [18], the load sharing can be formulated as:

$$p = (1-b)\,p_1 + bp_2 \tag{5}$$

$$q = (1-b)\,q_1 + bq_2 \tag{6}$$

$$\varepsilon = \varepsilon_1 = \varepsilon_2 \tag{7}$$

where, subscripts "$_1$" and "$_2$" apply to the elasto-brittle and elasto-plastic bodies respectively, and b is the cementation breakage ratio and represents the volume fraction of the elasto-plastic

81 body. The value b falls in the range of 0 to 1. Eqs. (5) and (6) can be rewritten into
82 corresponding incremental forms as:

$$\partial p = (1-b)\partial p_1 + b\partial p_2 + (p_2 - p_1)\partial b \tag{8}$$

$$\partial q = (1-b)\partial q_1 + b\partial q_2 + (q_2 - q_1)\partial b \tag{9}$$

83 Eqs. (8) and (9) suggest that p and q stress increments comprise three components: the stress
84 increment of elasto-brittle body, the stress increment of elasto-plastic body, and the stress
85 increment due to the cementation breakage. The three components are determined separately.
86
87 ***2.2.1 Stress increments of elasto-brittle body***
88 The stress increments of elastic-brittle body can be determined in terms of Hooke's law, as:

$$\partial p_1 = K_1 \partial \varepsilon_v \tag{10}$$

$$\partial q_1 = 3G_1 \partial \varepsilon_s \tag{11}$$

89 where K_1 is the material bulk modulus and is determined as the slope of line tangential to the
90 stress–strain curve obtained in an isotropic compression test, G_1 is the shear modulus and is the
91 slope of line tangential to the stress–strain curve obtained in a triaxial test, and ε_v and ε_s are the
92 volumetric strain and shear strain respectively and determined from the elasto-plastic body.
93
94 ***2.2.2 Stress increments of elasto-plastic body***
95 The stress increments of elasto-plastic body are determined in terms of model MCC [19]. This
96 model has been widely used to simulate elasto-plastic behavior of soil and other geomaterials.
97 As per [19], important forms are adopted in this section.
98
99 The volumetric and shear strains, ε_v and ε_s, consist of elastic and plastic components, and the
100 incremental forms are expressed as

$$\partial\varepsilon_v = \partial\varepsilon_v^e + \partial\varepsilon_v^p \tag{12}$$

$$\partial\varepsilon_s = \partial\varepsilon_s^e + \partial\varepsilon_s^p \tag{13}$$

where, $\partial\varepsilon_v^e$ and $\partial\varepsilon_s^e$ are the elastic components of volumetric and shear strains, respectively, $\partial\varepsilon_v^p$ and $\partial\varepsilon_s^p$ are the corresponding plastic components. The elastic components alone occur if the stress states for the elasto-plastic body sit inside the yield surface. Otherwise, yielding (or hardening) occurs. In the elastic stage, MCC defines the following stress–strain relationships:

$$\partial p_2 = \frac{(1+e)\,p_2}{\kappa}\left(\partial\varepsilon_v - \partial\varepsilon_v^p\right) \tag{14}$$

$$\partial q_2 = \frac{9(1-2\nu)}{2(1+\nu)}\left(\frac{(1+e)\,p_2}{\kappa}\right)\left(\partial\varepsilon_s - \partial\varepsilon_s^p\right) \tag{15}$$

where, e is the void ratio, κ is the slope of the swelling line, and ν is the Poisson's ratio.

MCC uses an elliptical yield locus, as in Figure 3. The yield surface is expressed as:

$$f\left(\boldsymbol{\sigma}, p_0\right) = {q_2}^2 + M^2 {p_2}^2 - M^2 p_2 p_0 \tag{16}$$

where M is the aspect ratio of the ellipse and determined as the slope of the critical state line (CSL); size of the locus, p_0, is the tip stress and is defined as the hardening parameter for the model. For general soils, MCC assumes an associated flow so that the plastic potential function uses the same form as the yield surface. However, as per [20], the plastic potential function causes discrepancy in plastic shear strain for cemented soils. To consider this, we adapted the associated flow into a non-associated one. In this sense, the plastic potential function is expressed as:

$$g(\boldsymbol{\sigma}) = {q_2}^2 + \alpha^2\left({p_2}^2 - {p_p}^2\right) \tag{17}$$

where α is the parameter used to determine the shape of the plastic potential, and p_p is the parameter for plastic potential scale. Both parameters are determined in terms of stress–strain curves and varied with the material ingredients in particular the cement content. Eq. (17) is presented in Figure 3. The form offers flexibility in shape and location and is applicable to greater varieties of stress–strain relationships. It is noteworthy that the setting of $\alpha = M$ and $p_p = \sqrt{p_2 p_0}$ simplifies the potential function into the yield locus.

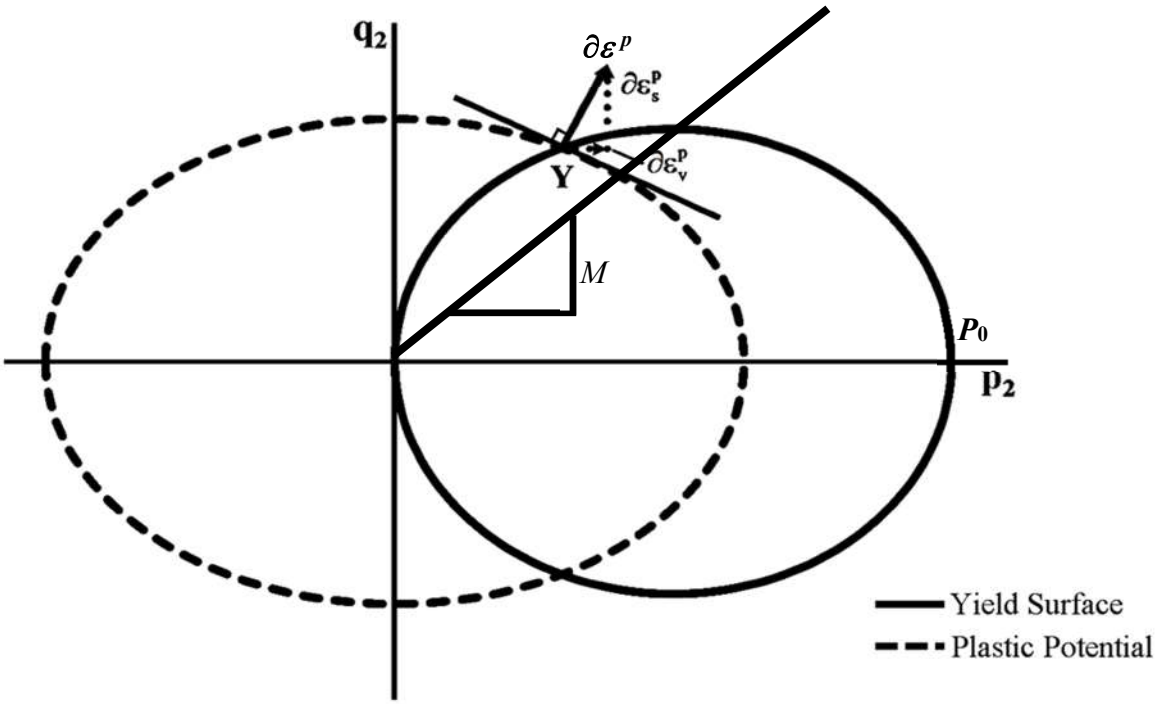

Figure 3 The non-associated flow in which the plastic potential curve is separate to the yield surface locus.

As an example, point *Y* in Figure 3 sits on the yield surface. Applying the hardening rule, the plastic strain increment vector, $\partial\varepsilon^p$, develops at a direction normal to the plastic potential locus. The plastic strain includes two components: the plastic volumetric strain, $\partial\varepsilon_v^p$, and the

130 plastic shear strain, $\partial\varepsilon_s^p$, which develop in parallel to the *p*- and *q*-axes respectively. Based on

131 the rule of normality, $\partial\varepsilon_v^p$ and $\partial\varepsilon_s^p$ can be expressed as:

$$\partial\varepsilon_v^p = \partial\theta \frac{\partial g}{\partial p_2} \tag{18}$$

$$\partial\varepsilon_s^p = \partial\theta \frac{\partial g}{\partial q_2} \tag{19}$$

132 where, $\partial\theta$ is a scalar multiplier and is determined in terms of the hardening trialed for the

133 material of interest; the other two terms are expressed as

$$\frac{\partial g}{\partial p_2} = 2\alpha^2 p_2 \tag{20}$$

$$\frac{\partial g}{\partial q_2} = 2q_2 \tag{21}$$

134 Combining Eqs. (18)–(21) yields:

$$\frac{\partial\varepsilon_s^p}{\partial\varepsilon_v^p} = \frac{\eta}{\alpha^2} \tag{22}$$

135 where the stress ratio $\eta = q_2/p_2$. Similarly, the strain vectors at other locations on the yield

136 locus are presented in Figure 4. Interestingly the vector directions suggest that shear contraction

137 occurs throughout the shear process where $\eta \neq 0$. The shear contraction suits the results in [5].

138

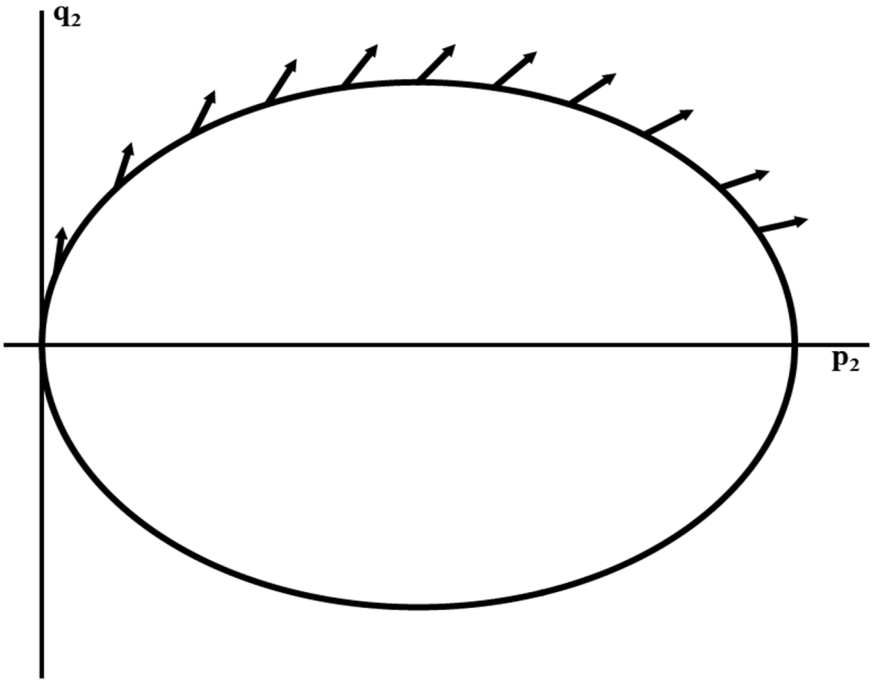

139

140

141 Figure 4 Normality of plastic strain increment vectors to yield locus.

142

143 The consistency equation for the yield surface Eq. (16) is expressed as:

$$\frac{\partial f}{\partial p_2}\partial p_2 + \frac{\partial f}{\partial q_2}\partial q_2 + \frac{\partial f}{\partial p_0}\partial p_0 = 0 \tag{23}$$

144 where

$$\frac{\partial f}{\partial p_2} = 2M^2 p_2 - M^2 p_0 \tag{24}$$

$$\frac{\partial f}{\partial q_2} = 2q_2 \tag{25}$$

$$\frac{\partial f}{\partial p_0} = -M^2 p_2 \tag{26}$$

145 Provided that the hardening rule, or the tip stress p_0, is dependent on the increments of plastic
146 volumetric strain and plastic shear strain, the change of the yield locus is linked to the changes
147 of both plastic volumetric strain and plastic shear strain, and thus is expressed as:

$$\partial p_0 = \frac{\partial p_0}{\partial \varepsilon_v^p}\partial \varepsilon_v^p + \frac{\partial p_0}{\partial \varepsilon_s^p}\partial \varepsilon_s^p \tag{27}$$

where $\partial \varepsilon_v^p$ and $\partial \varepsilon_s^p$ are provided in Eqs. (18)–(19). Substituting Eqs. (24)–(27) into Eq. (23), the scalar multiplier $\partial\theta$ is obtained as:

$$\partial\theta = -\frac{\dfrac{\partial f}{\partial p_2}\partial p_2 + \dfrac{\partial f}{\partial q_2}\partial q_2}{\dfrac{\partial f}{\partial p_0}\left(\dfrac{\partial p_0}{\partial \varepsilon_v^p}\dfrac{\partial g}{\partial p} + \dfrac{\partial p_0}{\partial \varepsilon_s^p}\dfrac{\partial g}{\partial q}\right)} \tag{28}$$

Substituting Eq. (28) into Eqs. (18) and (19), we have

$$\begin{bmatrix}\partial \varepsilon_v^p \\ \partial \varepsilon_s^p\end{bmatrix} = \frac{-1}{\left[\dfrac{\partial f}{\partial p_0}\left[\dfrac{\partial p_0}{\partial \varepsilon_v^p}\dfrac{\partial g}{\partial p_2} + \dfrac{\partial p_0}{\partial \varepsilon_s^p}\dfrac{\partial g}{\partial q_2}\right]\right]}\begin{bmatrix}\dfrac{\partial f}{\partial p_2}\dfrac{\partial g}{\partial p_2} & \dfrac{\partial f}{\partial q_2}\dfrac{\partial g}{\partial p_2} \\ \dfrac{\partial f}{\partial p_2}\dfrac{\partial g}{\partial q_2} & \dfrac{\partial f}{\partial q_2}\dfrac{\partial g}{\partial q_2}\end{bmatrix}\begin{bmatrix}\partial p_2 \\ \partial q_2\end{bmatrix} \tag{29}$$

where, from the isotropic compression, we have

$$\frac{\partial p_0}{\partial \varepsilon_v^p} = \frac{(1+e)p_0}{\lambda - \kappa} \tag{30}$$

$$\frac{\partial p_0}{\partial \varepsilon_s^p} = 0 \tag{31}$$

Substituting Eqs. (20), (21), (30) and (31) to Eq. (29), yields the plastic strain increments:

$$\begin{bmatrix}\partial \varepsilon_v^p \\ \partial \varepsilon_s^p\end{bmatrix} = \frac{\lambda - \kappa}{(1+e)\,p_2\left(M^2+\eta^2\right)\left(\alpha^2\right)}\begin{bmatrix}\alpha^2\left(M^2-\eta^2\right) & 2\eta\alpha^2 \\ \eta\left(M^2-\eta^2\right) & 2\eta^2\end{bmatrix}\begin{bmatrix}\partial p_2 \\ \partial q_2\end{bmatrix} \tag{32}$$

where λ is the slope of the CSL in v–ln$p$ plane.

2.2.3 Cementation breakage

The cementation breakage is defined by the breakage ratio b. As per [21], Weibull distribution is used to approximate b as:

$$b = 1 - e^{-(\varepsilon_d)^2} \tag{33}$$

where ε_d is the virtual damage strain and used as a measure of cementation breakage. As per [22], the damage strain is a function of volumetric and shear strains, and is expressed as

$$\varepsilon_d = \sqrt{{\varepsilon_v}^2 + {\varepsilon_s}^2} \tag{34}$$

The differential form for b can be expressed as:

$$\partial b = \frac{\partial b}{\partial \varepsilon_d}\left(\frac{\partial \varepsilon_d}{\partial \varepsilon_v}\partial \varepsilon_v + \frac{\partial \varepsilon_d}{\partial \varepsilon_s}\partial \varepsilon_s\right) = 2e^{-\left(\frac{\varepsilon_d}{\varepsilon_0}\right)^2}\left(\frac{1}{{\varepsilon_0}^2}\right)\left(\varepsilon_v \partial \varepsilon_v + \varepsilon_s \partial \varepsilon_s\right) \tag{35}$$

where ε_0 is a strain constant and expressed as:

$$\varepsilon_0 = \sqrt{\left(\frac{p_c}{K_1}\right)^2 + \left(\frac{q_c}{3G_1}\right)^2} \tag{36}$$

where p_c is mean yield stress, and q_c is deviatoric yield stress.

3. Model Implementation

The model is implemented to computer simulation. The key step is to develop a closed-form algorithm for the stress and strain increments. The algorithm can be developed in an explicit, implicit or combined form. The explicit form is time-forwarded and straight to implement, but as per [23] is vulnerable to yield incompliance. This concern can be corrected by running a trial in the implicit solution; the solutions however involve iterations which adds to computation cost. As per [24], we adopted a semi-implicit scheme, called the backward Euler return algorithm. This algorithm uses the first order of Taylor series of the yield equation and offers simplicity and efficiency.

The semi-implicit algorithm is illustrated in Figure 5. Point *X* that is in an elastic state represents the current stress. Point *Y* is trialed at a location beyond the current yield surface (i.e., $f > 0$). Stress path *XY* is virtually elastic. In terms of the constitutive relationships in Eqs. (14)−(15), stress increments *XY* are calculated as:

$$\partial {p_2}^{XY} = \frac{(1+e){p_2}^X}{\kappa}\partial \varepsilon_v \tag{37}$$

$$\partial {q_2}^{XY} = \frac{9(1-2\nu)}{2(1+\nu)}\left(\frac{(1+e){p_2}^X}{\kappa}\right)\partial \varepsilon_s \tag{38}$$

178 The stresses at *Y* are updated as:

$${p_2}^Y = {p_2}^X + \partial {p_2}^{XY} \tag{39}$$

$${q_2}^Y = {q_2}^X + \partial {q_2}^{XY} \tag{40}$$

179 Fitting the updated stresses to the yield surface as in Eq. (16), gives

$$f^Y = f({p_2}^Y,\ {q_2}^Y) \tag{41}$$

180 The first order of Taylor series of Eq. (41) is expressed as

$$f = f^Y + \frac{\partial f}{\partial p_2}\partial p_2 + \frac{\partial f}{\partial q_2}\partial q_2 + \frac{\partial f}{\partial p_0}\partial p_0 \tag{42}$$

181 Applying the flow rule Eqs. (18) and (19) to Eq. (42), we have

$$f = f^Y - \left(\frac{(1+e)({p_2}^Y)^2(M^2-\eta^2)}{\kappa}\frac{\partial g}{\partial p_2} + \frac{9(1-2\nu)}{2(1+\nu)}\left(\frac{(1+e)2{p_2}^Y{q_2}^Y}{\kappa}\right)\frac{\partial g}{\partial q_2} + \frac{(1+e)({p_2}^Y)^2(M^2+\eta^2)}{\lambda-\kappa}\frac{\partial g}{\partial p_2}\right)\partial\theta \tag{43}$$

182 On stress path *XY*, applying yielding condition $f = 0$ to Eq. (43) gives rise to yield location point

183 *Z*. Considering Eq. (28), the scalar multiplier $\partial\theta$ is obtained as:

$$\partial\theta = \frac{f^Y}{\left(\frac{2\alpha^2(1+e)({p_2}^Y)^3(M^2-\eta^2)}{\kappa} + \frac{9(1-2\nu)}{2(1+\nu)}\left(\frac{(1+e)4{p_2}^Y({q_2}^Y)^2}{\kappa}\right) + \frac{2\alpha^2(1+e)({p_2}^Y)^3(M^2+\eta^2)}{\lambda-\kappa}\right)} \tag{44}$$

184 Substituting Eq. (44) back to Eqs. (18) and (19), stress increments *YZ* are expressed as

$$\partial {p_2}^{YZ} = -\frac{2\alpha^2(1+e)({p_2}^Y)^2}{\kappa}\partial\theta \tag{45}$$

$$\partial {q_2}^{YZ} = -\frac{9(1-2\nu)}{2(1+\nu)}\left(\frac{2(1+e){p_2}^Y{q_2}^Y}{\kappa}\right)\partial\theta \tag{46}$$

185 The negative values agree with the stresses overestimated for the trial and should be deducted
186 to attain stress state at location *Z*. The stress increments are updated as:

$$\partial p_2 = \partial {p_2}^{XY} + \partial {p_2}^{YZ} \tag{47}$$

$$\partial q_2 = \partial {q_2}^{XY} + \partial {q_2}^{YZ} \tag{48}$$

187 Substituting Eqs. (47) and (48) to the total stress incremental forms in Eqs. (8) and (9), the total
188 stress increments become:

$$\partial p = (1-b)K_1 \partial \varepsilon_v + b\partial {p_2}^{XY} + b\partial {p_2}^{YZ} + \partial b({p_2}^X - {p_1}^X) \tag{49}$$

$$\partial q = 3(1-b)G_1 \partial \varepsilon_s + b\partial {q_2}^{XY} + b\partial {q_2}^{YZ} + \partial b({q_2}^X - {q_1}^X) \tag{50}$$

189 It is noteworthy that point *Z* may not lie on the new yield surface, i.e., $f\left({p_2}^Z, {q_2}^Z\right) \neq 0$. The
190 algorithm can be improved by dividing the strain increment into *n* sub-increments, at locations
191 Y_1, Y_2,…, Y_{n+1}, and by applying the stress-return algorithm to each sub-increment. By applying
192 the semi-implicit algorithm to each single sub-increment, the stresses at point *Z* as in Eqs. (47)
193 and (48) are determined as:

$$\partial p_2 = \partial {p_2}^{XY_1} + \partial {p_2}^{Y_1Y_2} + \partial {p_2}^{Y_2Y_3} + \cdots + \partial {p_2}^{Y_nY_{n+1}} + \partial {p_2}^{Y_{n+1}Z} \tag{51}$$

$$\partial q_2 = \partial {q_2}^{XY_1} + \partial {q_2}^{Y_1Y_2} + \partial {q_2}^{Y_2Y_3} + \cdots + \partial {q_2}^{Y_nY_{n+1}} + \partial {q_2}^{Y_{n+1}Z} \tag{52}$$

194

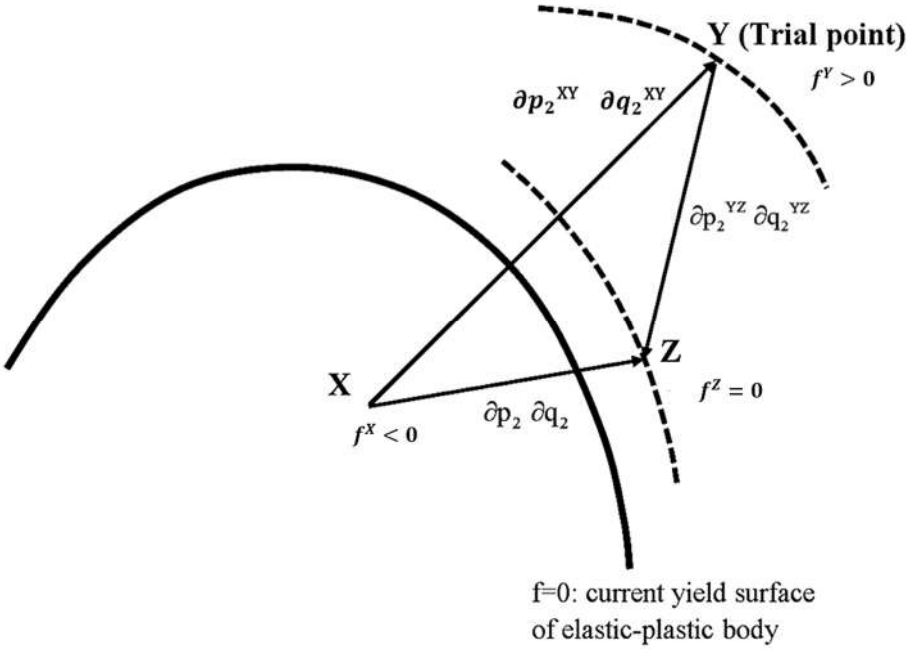

Figure 5 Schematic of the semi-implicit scheme where point *X* is in the elastic state, point *Y* is beyond the yield surface; from points *X* and *Y* point *Z* on the yield surface is determined.

4. Model Verification

The model was verified in a laboratory test. Triaxial tests were conducted on cemented backfills that comprised waste foundry sand, EPS beads class-F fly ash, cement and water, with ingredients dosage provided in Table 1. The EPS beads are compressible, but super-lightweight enabling weight reduction by up to 36% depending on the dosages [5, 25]. The test samples are shown in Figure 6. Further sample details, including dosage, physical properties and mechanical behavior, are provided in [1, 5].

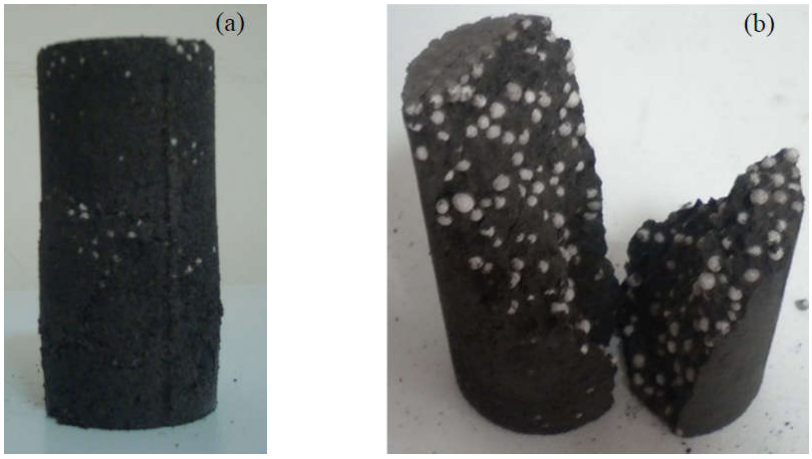

Figure 6 Cemented EPS backfill samples: (a) before triaxal test, (b) after triaxal test, with the white color EPS beads incorporated in the waste foundry sand base material.

Table 1 Dosage of cemented EPS-backfill sample used for triaxial tests.

Ingredient	Dosage
Cement (kg/m^3)	50
Fly ash (kg/m^3)	448.5
Foundry sand (kg/m^3)	500
EPS bead (kg/m^3)	4.21
Water (kg/m^3)	280

The samples were subjected to isotropic tests and consolidated drained (CD) triaxial tests respectively. In the CD tests, three confinements were used: 100, 200 and 300 kPa. The test procedure and results were provided in [5]. The model input parameters that were obtained from the tests are provided in Table 2. The model parameters are applied to the model and algorithm that have been developed for the material, thus enabling simulation of stress–strain relationships.

220 Table 2 Model parameters for cemented EPS backfill samples.

Parameter	Value
Mean yield stress, $p_c = p_0$ (kPa)	79.6
Deviatoric yield stress, q_c (kPa)	324.8
Bulk modulus, K_1 (MPa)	6.3
Shear modulus, G_1 (MPa)	3.5
Slope of CSL in p–q plane, M	1.11
Slope of CSL in v–ln$p$ plane, λ	0.04
Slope of swelling line, κ	0.003
Initial void ratio, e_0	0.89
Plastic potential parameter, α	0.60
Plastic potential parameter, p_p	50

221

222 The stress–strain relationships are provided in Figure 7. The results include the deviator stress,
223 volumetric strain and axial strain obtained from the tests, and simulations obtained from MCC
224 model and the model developed in this study. Better agreement between the test and current
225 model simulation results is attained. The agreement applies to the initial linear, mid-stage
226 yielding and late-stage plastic sections of the stress–strain curves, for the three confinements
227 acted on the samples. Specifically, the elastic-brittle body replicates material stiffening
228 initially; the stiffness is held up until cementation breakage evolves; and the breakage evolves
229 at a ratio which gauges trajectory at mid- to late stages. More importantly, the proposed plastic
230 potential enables capturing shear contraction more appropriately than MCC model does in all
231 three tests. A better simulation of volumetric strains is obtained from applying the non-associated flow
232 rule which allows the volumetric strain to continue evolving after the material has reaches the critical
233 state. In contrast, the volumetric strain becomes constant at critical state if MCC model is used. These

advantages corroborate the development of the modified flow rule and verifies the capability of the model in approximating ductile behavior of EPS-based backfills. Small discrepancy occurs to the deviatoric stresses obtained at relatively high axial strain stage (e.g., 5% or above) under the relatively high confinements (e.g., 200 kPa or above). Albeit the discrepancy, the current model captures trends of shear behavior, in particularly, at the early- to mid-stages and can be used to predict mechanical responses of the material.

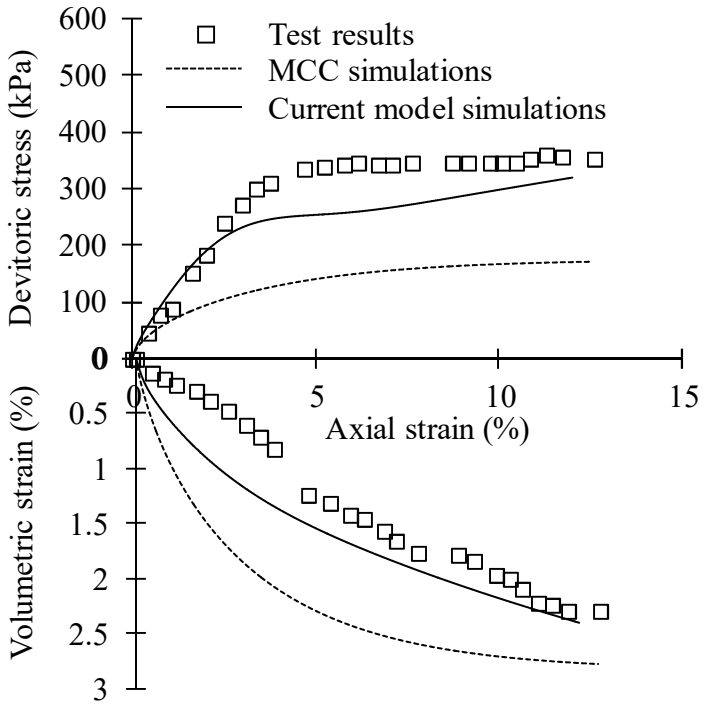

(a)

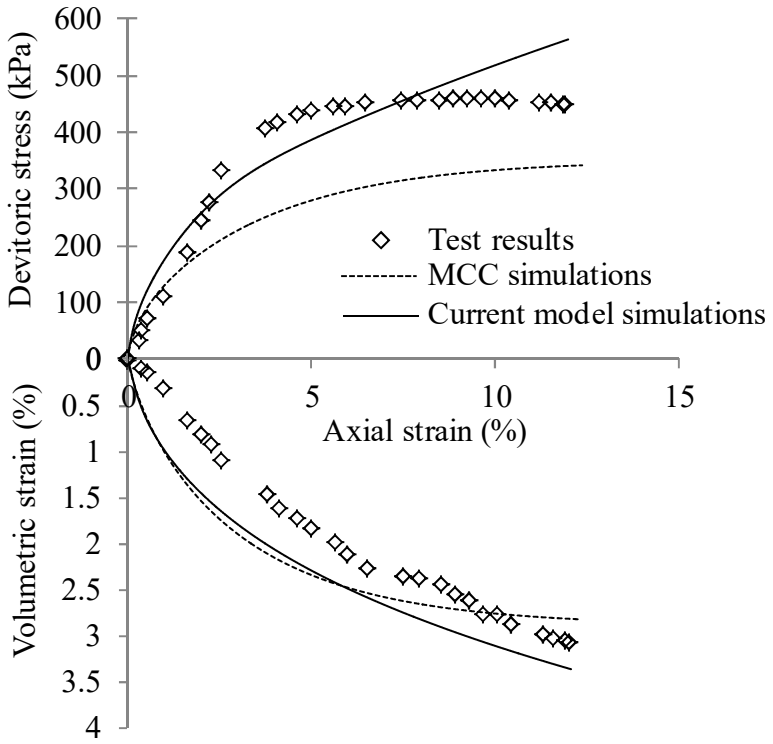
Devitoric stress (kPa)
600
500
400
300
200
100
0
Test results
MCC simulations
Current model simulations
0
5
10
15
Axial strain (%)
Volumetric strain (%)
0
0.5
1
1.5
2
2.5
3
3.5
4

243

244 (b)

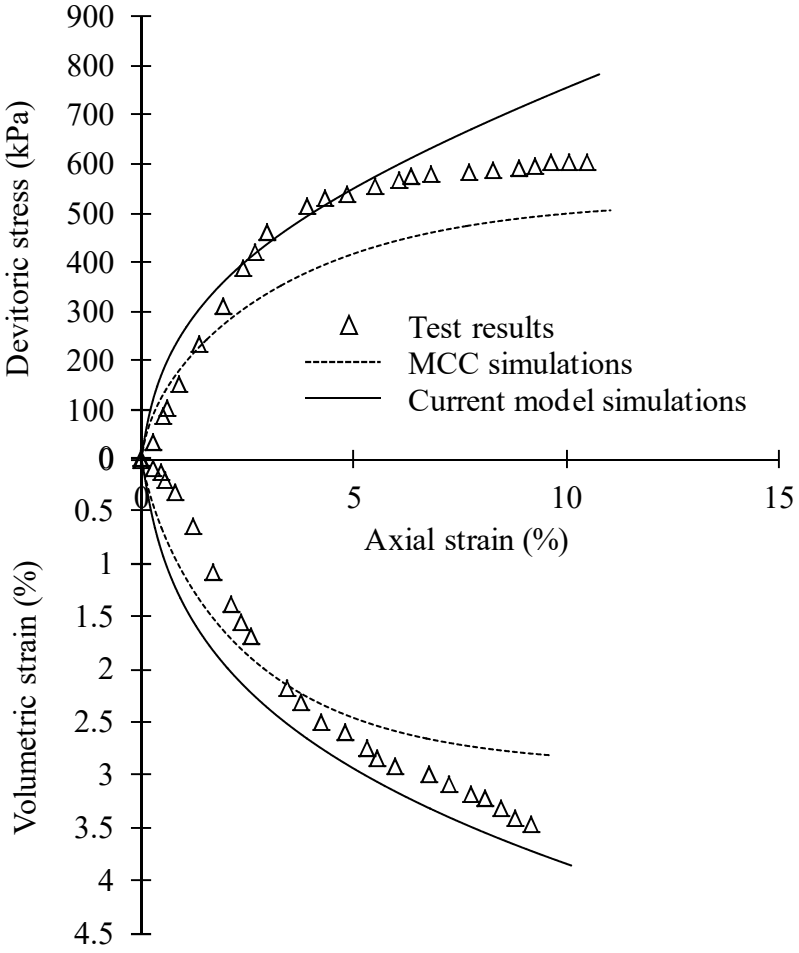
Devitoric stress (kPa)
900
800
700
600
500
400
300
200
100
0
Test results
MCC simulations
Current model simulations
0
5
10
15
Axial strain (%)
Volumetric strain (%)
0
0.5
1
1.5
2
2.5
3
3.5
4
4.5

245

(c)

Figure 7: Deviatoric stress, volumetric strain and axial strain results obtained for cemented EPS backfill samples that are subjected to triaxial tests under confinements: (a) 100 kPa, (b) 200 kPa and (c) 300 kPa.

To gain further insight into the model, the stress paths in $p-q$ plane are provided in Figure 8. The figure includes two sets of stress path graphs. Figure 8(a) presents the overall stresses acted on the entire samples, i.e., the stresses taken by the combination of elasto-brittle and elasto-plastic bodies. Figure 8(b) shows the component stresses that are withstood by the elasto-plastic body alone. Due to the object difference, the overall stress paths follow the $\Delta q/\Delta p=3$ lines as for the drained triaxial tests; the component stress paths for the elasto-plastic body, which nominally represents part of the sample, do not develop at the $\Delta q/\Delta p=3$ gradient, but are curvy and confinement dependent, reflecting nonlinearity of cementation breakage. Highlights are: i) the overall and the component stress paths approach the CSL, suggesting breakage completion and take-over of the elasto-plastic body at the end; and ii) elasto-plastic body takes over earlier under 300 kPa confinement than 200 or 100 kPa.

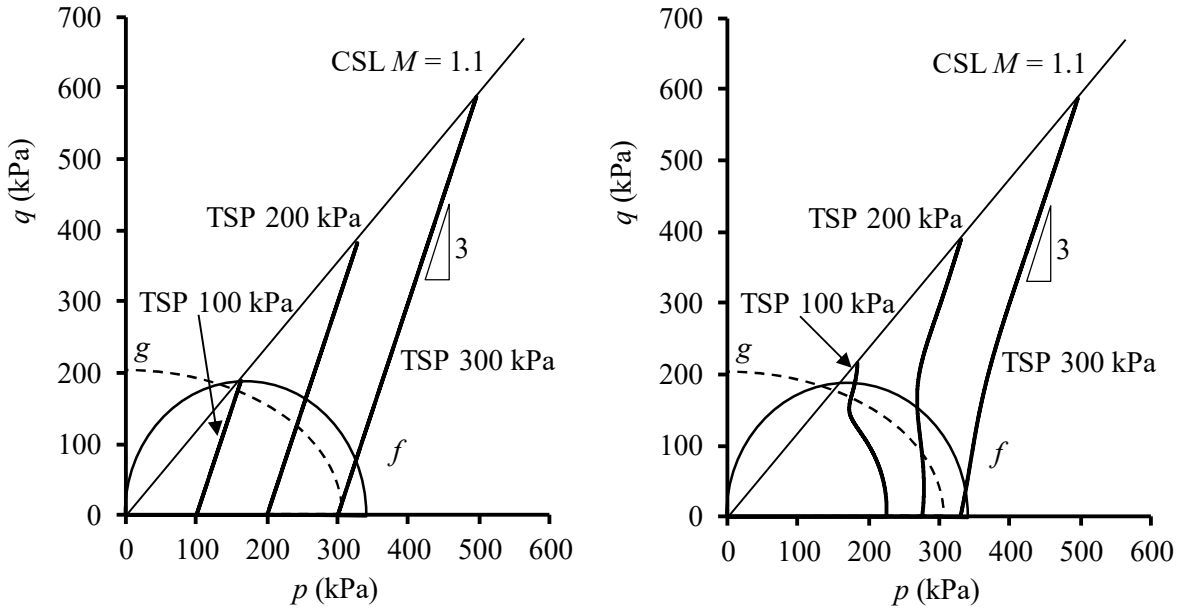

Figure 8: Stress paths for: (a) the combination of the elasto-brittle and elasto-plastic bodies; (b) the elasto-plastic body alone.

5. Conclusions

An analytical model that was developed for cemented backfills is presented. The model considers the combined elastic, plastic and brittle behaviors of the material. The collective behavior is approximated by using an elasto-brittle body and an elasto-plastic body in parallel, thus enabling simulation of progressive breakage of cementation structure. The model uses a non-associated flow rule to assess hardening. This non-associated flow rule allows for greater flexibility in reproducing material stress–strain relationships. The model introduces a semi-implicit form for the time step and determines the stress increments more preciously. The above formulation enables the model to simulate complex shear behavior, including ductility and contraction, for materials containing compressible inclusions. The model was verified on a lightweight cemented backfill that incorporated expanded polyethylene beads.

Acknowledgement

This work was supported by Australian Research Council (DP140103004).

Notations

b	breakage ratio
e	void ratio
f	yield locus
f_y	yield strength
g	plastic potential locus
G_1	shear modulus
K_1	bulk modulus
M	slope of CSL in p–q plane
p	mean stress
p_0	tip stress hardening parameter
p_1	mean stress shared by elasto–brittle body
p_2	mean stress shared by elasto–plastic body
p_c	mean yield stress
p_p	parameter used to define magnitude of plastic potential
q	deviatoric stress
q_1	deviatoric stress shared by elasto-brittle body
q_2	deviatoric stress shared by elasto-plastic body
q_c	deviatoric yield stress
q_u	break strength
t	time step
α	parameter used to determine shape of plastic potential
σ_1	major principal stress

306 σ_3 minor principal stress

307 ε strain

308 ε_0 strain constant

309 ε_1 strain of elasto-brittle body

310 ε_2 strain of elasto-plastic body

311 ε_d virtual damage strain

312 ε_s shear strain

313 ε_v volumetric strain

314 ε_s^e elastic components of shear strain

315 ε_v^e elastic component of volumetric strain

316 ε_s^p plastic components of shear strain

317 ε_v^p plastic component of volumetric strain

318 λ slope of CSL

319 κ slope of swelling line

320 ν Poisson's ratio

321 η stress ratio of q_2/p_2

322 $\partial\theta$ scalar multiplier

323

324 **References**

325 [1] Liu HL, Deng A, Chu J. Effect of different mixing ratios of polystyrene pre-puff beads

326 and cement on the mechanical behaviour of lightweight fill. Geotextiles and Geomembranes.

327 2006;24(6):331-8.

[2] Wang C, Deng A, Taheri A. Digital Image Processing on Segregation of Rubber Sand Mixture. Int J Geomech. 2018;18(10).

[3] Soltani A, Deng A, Taheri A, Mirzababaei M. Rubber powder-polymer combined stabilization of South Australian expansive soils. Geosynth Int. 2018;25(3):304-21.

[4] Wang C, Deng A, Taheri A. Three-dimensional discrete element modeling of direct shear test for granular rubber-sand. Comput Geotech. 2018;97(204-16.

[5] Deng A, Feng J. Modeling mechanical response of cemented EPS-backfill. Congress on Stability and Performance of Slopes and Embankments (2013: San Diego)2013.

[6] Horpibulsuk S, Rachan R, Suddeepong A, Liu MD, Du YJ. Compressibility of lightweight cemented clays. Engineering Geology. 2013;159(59-66.

[7] Tsoi WY, Lee KM. Mechanical properties of cemented scrap rubber tyre chips. Geotechnique. 2011;61(2):133-41.

[8] Yu HS, Tan SM, Schnaid F. A critical state framework for modelling bonded geomaterials. Geomechanics and Geoengineering. 2007;2(1):61-74.

[9] Ge L, Hwang YW, Sun H, He GD, Chen R, Kang X. Effective tensile strength of lightly cemented sand. Journal of Materials in Civil Engineering. 2019;31(1).

[10] Gens A, Nova R. Conceptual bases for a constitutive model for bonded soils and weak rocks. In: al. Ae, editor. Proc Geotechnical Engineering Hard Soils-Soft Rocks. Athens: Balkema, 1993. p. 485-94.

[11] Rahimi M, Chan D, Nouri A. Bounding surface constitutive model for cemented sand under monotonic loading. Int J Geomech. 2015:04015049.

[12] Burland J. On the compressibility and shear strength of natural clays. Géotechnique. 1990;40(3):329-78.

[13] Chun BS, Lim HS, Sagong M, Kim K. Development of a hyperbolic constitutive model for expanded polystyrene (EPS) geofoam under triaxial compression tests. Geotextiles and Geomembranes. 2004;22(4):223-37.

[14] Hazarika H, Okuzono S. Modeling the behavior of a hybrid interactive system involving soil, structure and EPS geofoam. Soils Found. 2004;44(5):149-62.

[15] Wong H, Leo CJ. A simple elastoplastic hardening constitutive model for EPS geofoam. Geotextiles and Geomembranes. 2006;24(5):299-310.

[16] Hazarika H. Stress-strain modeling of EPS geofoam for large-strain applications. Geotextiles and Geomembranes. 2006;24(2):79-90.

[17] Jiang MJ, Yu HS, Harris D. Bond rolling resistance and its effect on yielding of bonded granulates by DEM analyses. International Journal for Numerical and Analytical Methods in Geomechanics. 2006;30(8):723-61.

[18] Wang JG, Leung CF, Ichikawa Y. A simplified homogenisation method for composite soils. Comput Geotech. 2002;29(6):477-500.

[19] Roscoe K, Burland K. On the generalised stress-strain behaviour of wet clay. In: Jeyman J, Leckie F, editors. Engineering Plasticity. Cambridge UK: Cambridge University Press, 1968. p. 535-609.

[20] Horpibulsuk S, Liu MD, Liyanapathirana DS, Suebsuk J. Behaviour of cemented clay simulated via the theoretical framework of the Structured Cam Clay model. Comput Geotech. 2010;37(1):1-9.

[21] Shen Z-J. Progress in binary medium modeling of geological materials: Springer, 2006.

[22] Kavvadas M, Amorosi A. A constitutive model for structured soils. Géotechnique. 2000;50(3):263-73.

[23] Dunne F, Petrinic N. Introduction to computational plasticity: Oxford University Press New York, 2005.

376 [24] Simo JC. Numerical analysis and simulation of plasticity. Handbook of numerical
377 analysis. 1998;6(183-499.
378 [25] Deng A, Xiao Y. Measuring and modeling proportion-dependent stress-strain behavior
379 of EPS-sand mixture. Int J Geomech. 2010;10(6):214-22.

380